IEEE Access
Multidisciplinary | Rapid Review | Open Access Journal

Received July 14, 2020, accepted July 22, 2020, date of publication July 29, 2020, date of current version August 10, 2020.

Digital Object Identifier 10.1109/ACCESS.2020.3012706

A Novel Hardware-Efficient Central Pattern Generator Model Based on Asynchronous Cellular Automaton Dynamics for Controlling Hexapod Robot

KENTARO TAKEDA, (Graduate Student Member, IEEE), AND HIROYUKI TORIKAI, (Member, IEEE)
Graduate School of Science and Engineering, Hosei University, Tokyo 184-8594, Japan
Corresponding author: Kentaro Takeda (takeda@mail.nsci.jp)

This work was supported by JSPS KAKENHI under Grant 19J20745 and Grant 18K11482.

ABSTRACT This paper presents a novel hardware-efficient central pattern generator (CPG) model to realize a bio-inspired gait of a hexapod robot. The CPG model consists of a network of cellular automaton (CA) oscillators; thus, it can be implemented as a network of sequential logic circuits. Detailed analyses of nonlinear oscillation dynamics show that the oscillator that is driven by multiple asynchronous clocks is more suitable to realize the gait of the robot than an oscillator that is driven by a single clock or multiple synchronous clocks. Moreover, detailed analyses of nonlinear network dynamics show that the clocks among the CA oscillators should be asynchronous to appropriately realize the gait. Using the analyses, systematic procedures to design the CPG model are proposed. The proposed CPG model is implemented in a field programmable gate array (FPGA); our experiments validate that the CPG model implemented in an FPGA can realize the bio-inspired gait of a hardware robot. Further, we show that the proposed CPG model utilizes fewer circuit elements and lower power than a conventional CPG model.

INDEX TERMS Asynchronous cellular automaton, central pattern generator (CPG), field programmable gate array (FPGA), hexapod robot, nonlinear dynamics, synchronization.

I. INTRODUCTION

Various species of animals, such as ants, spiders, snakes, and fish perform locomotion using flexor and extensor muscles that are driven by multiple signals with rhythmic patterns. Studies in the field of biological motor control system show that such rhythmic patterns are produced by central pattern generators (CPGs) in the central nervous systems [1]. Inspired by this biological principle, many mathematical and electronic circuit models of CPGs have been designed to control artificial robots that are capable of performing useful tasks [2], [3]. For example, networks of Hopf and Kuramoto oscillators have been used to control hexapod robots, as shown in Fig. 1. Further, CPG models have been used in the field of medical engineering [4], [5]. For example, a network of integrate-and-fire oscillators were used to control mammalian muscles to assist in damaged nervous systems [5]. Considering the nonlinear circuit and system theory, biomimetic models, including the CPG models, are classified into the following four classes based on continuousness and discontinuousness of state variable and time.

Class CTCS. This is a nonlinear differential equation model of a biomimetic system with *a continuous time and continuous states* (CTCS). A class CTCS biomimetic model can be generally implemented in an analog nonlinear circuit, e.g., [5]–[9].

Class DTCS. This is a nonlinear difference equation model of a biomimetic system with *a discrete time and continuous states* (DTCS). A class DTCS biomimetic model can be generally implemented in a switched capacitor circuit, e.g., [10]–[13].

Class DTDS. This is a numerical integration model (in finite binary number representation) of a biomimetic system with *a discrete time and discrete states* (DTDS). A class

The associate editor coordinating the review of this manuscript and approving it for publication was Norbert Herencsar.

This work is licensed under a Creative Commons Attribution 4.0 License. For more information, see https://creativecommons.org/licenses/by/4.0/

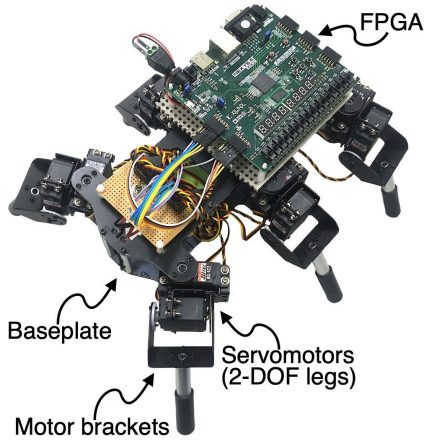

FIGURE 1. Hexapod robot [38] mounted with a field programmable gate array (FPGA) with the proposed central pattern generator (CPG) model.

DTDS biomimetic model can be generally implemented in a digital processor or a biomimetic sequential logic circuit, e.g., [14]–[19].

Class CTDS. This is an asynchronous cellular automaton (CA) model of a biomimetic system with *a continuous (state transition) time and discrete states* (CTDS). A class CTDS biomimetic model can be generally implemented in an asynchronous sequential logic circuit, e.g., [20]–[36].

Most conventional biomimetic models belong to the CTCS, DTCS, and DTDS classes. The CPG models in [5]–[8], [10]–[12], and [14]–[18] belong to the CTCS, DTCS, and DTDS classes, respectively. We and certain other research groups have been developing various kinds of class CTDS biomimetic models, e.g.,

- Asynchronous CA neuron models [20]–[23],
- Asynchronous CA cochlea models [24]–[27],
- Asynchronous CA gene–protein system models [28],
- Asynchronous CA neural network models [29]–[32],
- Asynchronous CA CPG models [33], [34].

These studies have shown that class CTDS biomimetic models have many advantages, such as the following: (i) The models can be implemented by fewer circuit elements than the numerical integration models employed in digital processors [20]–[34], and (ii) They consume lower power than numerical integration models employed in digital processors [20]–[34]. Hence, this study aims at presenting a novel asynchronous CA model of the CPG that consumes fewer circuit elements and lower power than a conventional digital processor CPG model.

Fig. 2(a) shows a conceptual diagram of the proposed CPG model, where each oscillator is implemented in a sequential logic circuit; thus, its dynamics is described by a CA. In this study, a CA oscillator is introduced in Section II. Detailed analyses of nonlinear dynamics of the CA oscillator reveal an important advantage of the asynchronous nature of the clocks: an asynchronous CA oscillator (i.e., a CA oscillator with multiple asynchronous clocks) can control its oscillation such that the oscillation is suited to control a hexapod robot, while a

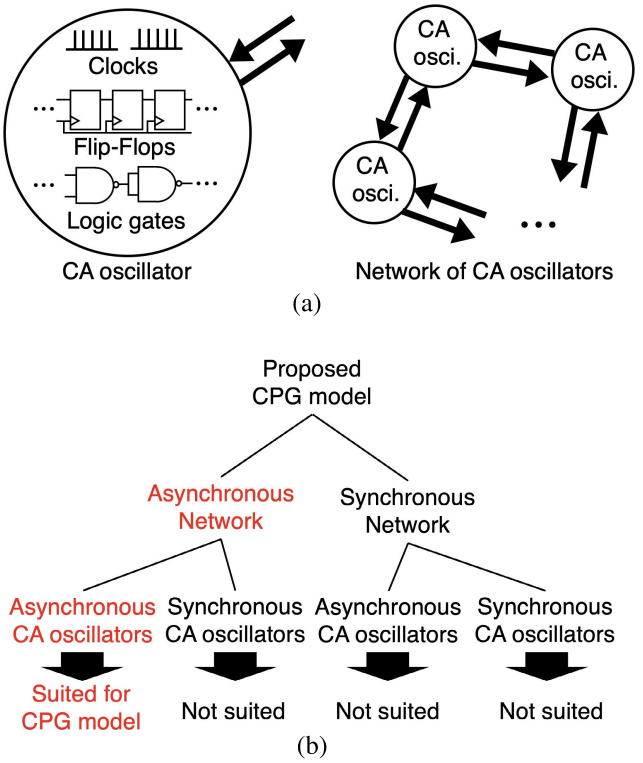

FIGURE 2. Cellular automaton oscillator and four types of networks.

synchronous CA oscillator (i.e., a CA oscillator with a single clock or multiple synchronous clocks) cannot. As preparations to design the CPG, Section III presents a small network of the CA oscillators. Detailed analyses of the nonlinear dynamics of the network reveal the effects of the parameters on the synchronization phenomena of the network. Section IV presents a novel asynchronous CA CPG model, which consists of a network of CA oscillators. Depending on the asynchronous nature of the clocks *in a single CA oscillator* and *among multiple CA oscillators*, the following four types of CA oscillator networks exist (see also Fig. 2(b)).

(a) *Asynchronous network of asynchronous CA oscillators*
(b) *Synchronous network of asynchronous CA oscillators*
(c) *Asynchronous network of synchronous CA oscillators*
(d) *Synchronous network of synchronous CA oscillators*

Detailed analyses of nonlinear dynamics of the four networks reveal that the *asynchronous network of asynchronous CA oscillators* is best suited to be employed as a CPG model. Based on the aforementioned analyses, systematic design procedures of the CPG model are proposed. In Section V, the proposed CPG model is implemented in a field programmable gate array (FPGA). Our experiments indicate that the CPG model implemented in an FPGA can realize a tripod gait of the hardware robot, as shown in Fig. 1, where the tripod gait is a typical gait observed in six-legged insects [37]. For comparison, a conventional digital processor CPG model is implemented in the same FPGA. It is observed that the proposed CPG model employs fewer circuit elements and

lower power than the conventional CPG model. This paper reports the following novelties and significances.

- This study proposes a novel CPG model design procedure, which employs few circuit elements and low power. Hence, this study provides fundamental measures to develop small and low-power CPG models, whose potential applications include single-chip low-power controllers for bio-inspired multi-legged robots and implantable muscle controllers to assist in damaged nervous systems.
- This study analyzes the effects of the asynchronous nature of clocks in the CA oscillators in a network. To the best of our knowledge, this analysis has been performed for the first time. Hence, this study can contribute to develop *new nonlinear circuit theories – oscillation and synchronization theories of networks of asynchronous sequential logic circuits.*
- Although preliminary results of this study were presented in an IEEE flagship conference [33], to the best of our knowledge, this paper reports detailed analyses of a CA oscillator and its networks for the first time. These analyses reveal that the network in this study is better suited to be employed as a CPG than the previously reported network.

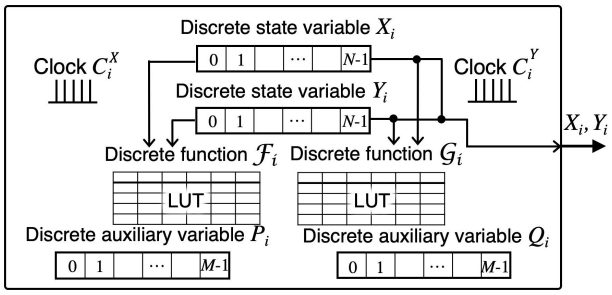

FIGURE 3. Schematic diagram of the asynchronous cellular automaton (CA) oscillator. LUT represents look-up table.

II. ASYNCHRONOUS CA OSCILLATOR

A. MODEL DESCRIPTION

This subsection describes an asynchronous CA oscillator, which is used as an element of a CPG model, as described in a further section. Fig. 3 shows a schematic diagram of the CA oscillator. The CA oscillator has two clocks

$$C_i^X(t) = \sum_{k=0}^{\infty} \delta(t - kT_i^X),$$

$$C_i^Y(t) = \sum_{k=0}^{\infty} \delta(t - kT_i^Y),$$

where i is an oscillator index, $t \in \mathbb{R}$ is a continuous time, $T_i^X \in (0, \infty)$ and $T_i^Y \in (0, \infty)$ are clock periods, and $\delta : \mathbb{R} \to \{0, 1\}$ is the unit impulse function

$$\delta(t) = \begin{cases} 1 & \text{if } t = 0, \\ 0 & \text{if } t \neq 0. \end{cases}$$

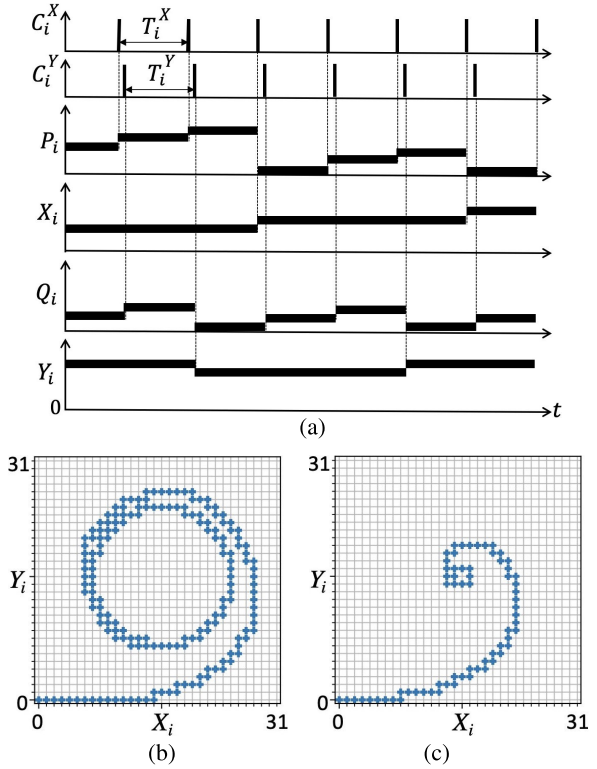

FIGURE 4. Nonlinear dynamics of the CA oscillator. $N = 2^5$, $M = 2^{10}$, $\omega_i = 2\pi/\alpha_i$, $\alpha_i = 0.01$, $T_i^X = 0.001$, and $T_i^Y = 0.001014142$. (a) Timing chart of state transitions. (b) Phase plane trajectory starting from $X_i = Y_i = P_i = Q_i = 0$. $\rho_i = 144$. (c) Phase plane trajectory starting from $X_i = Y_i = P_i = Q_i = 0$. $\rho_i = -100$.

Further, as shown in Fig. 3, the CA oscillator has the following two discrete state variables $\{X_i, Y_i\}$ and two discrete auxiliary variables $\{P_i, Q_i\}$.

$$X_i \in \mathbf{Z}_N \equiv \{0, \cdots, N-1\}, \quad Y_i \in \mathbf{Z}_N, \tag{1}$$

$$P_i \in \mathbf{Z}_M \equiv \{0, \cdots, M-1\}, \quad Q_i \in \mathbf{Z}_M, \tag{2}$$

where N and M are positive integers characterizing resolutions of the discrete state variables X_i,Y_i, P_i, and Q_i. The two clocks C_i^X and C_i^Y trigger transitions of the discrete state variables X_i and Y_i as follows (see Fig. 4(a)).

$$\text{If } C_i^X(t) = 1 \text{ and } P_i(t) \geq |\mathcal{F}_i(X_i(t), Y_i(t))|, \text{ then}$$

$$X_i(t_+) := \begin{cases} X_i(t) + 1 & \text{if } \mathcal{F}_i(X_i(t), Y_i(t)) \geq 0 \text{ and} \\ & X_i(t) < N - 1, \\ X_i(t) - 1 & \text{if } \mathcal{F}_i(X_i(t), Y_i(t)) < 0 \text{ and} \\ & X_i(t) > 0. \end{cases}$$

$$\text{If } C_i^Y(t) = 1 \text{ and } Q_i(t) \geq |\mathcal{G}_i(X_i(t), Y_i(t))|, \text{ then} \tag{3}$$

$$Y_i(t_+) := \begin{cases} Y_i(t) + 1 & \text{if } \mathcal{G}_i(X_i(t), Y_i(t)) \geq 0 \text{ and} \\ & Y_i(t) < N - 1, \\ Y_i(t) - 1 & \text{if } \mathcal{G}_i(X_i(t), Y_i(t)) < 0 \text{ and} \\ & Y_i(t) > 0, \end{cases} \tag{4}$$

where "t_+" denotes "$\lim_{\epsilon \to +0} t + \epsilon$" and ":=" denotes an "instantaneous state transition." Moreover, $\mathcal{F}_i : \mathbf{Z}_N \times \mathbf{Z}_N \to$

$\boldsymbol{Z}_M^{\pm} \equiv \{-(M-1), \cdots, (M-1)\}$ and $\mathcal{G}_i : \boldsymbol{Z}_N \times \boldsymbol{Z}_N \to \boldsymbol{Z}_M^{\pm}$ denote discrete functions

$$\mathcal{F}_i \equiv F_i \circ f_i, \quad \mathcal{G}_i \equiv G_i \circ g_i, \tag{5}$$

where $\mathcal{F}_i$ and $\mathcal{G}_i$ are implemented in look-up-tables, as shown in Fig. 3. In this study, we propose to design the functions $F_i : \mathbb{R} \to \boldsymbol{Z}_M^{\pm}$ and $G_i : \mathbb{R} \to \boldsymbol{Z}_M^{\pm}$ as follows.

$$F_i(x) = \left\lfloor \frac{1}{\alpha_i T_i^X x} \right\rfloor, \; G_i(y) = \left\lfloor \frac{1}{\alpha_i T_i^Y y} \right\rfloor,$$

where the functions F_i and G_i are assumed to be saturated at $\pm(M-1)$, $\alpha_i \in (0, \infty)$ is a scaling parameter, and $\lfloor . \rfloor$ denotes the floor function

$$\lfloor z \rfloor = \max\{n \in \mathbb{Z} \mid n \le z\}.$$

Further, we propose to design the functions $f_i : \boldsymbol{Z}_N \times \boldsymbol{Z}_N \to \mathbb{R}$ and $g_i : \boldsymbol{Z}_N \times \boldsymbol{Z}_N \to \mathbb{R}$ as follows.

$$\begin{aligned} f_i(x,y) &= \rho_i\Big(x - \Big\lfloor \frac{N}{2} \Big\rfloor\Big) - \omega_i\Big(y - \Big\lfloor \frac{N}{2} \Big\rfloor\Big) \\ &\quad - \Big(x - \Big\lfloor \frac{N}{2} \Big\rfloor\Big)\Big(\Big(x - \Big\lfloor \frac{N}{2} \Big\rfloor\Big)^2 + \Big(y - \Big\lfloor \frac{N}{2} \Big\rfloor\Big)^2\Big), \\ g_i(x,y) &= \omega_i\Big(x - \Big\lfloor \frac{N}{2} \Big\rfloor\Big) + \rho_i\Big(y - \Big\lfloor \frac{N}{2} \Big\rfloor\Big) \\ &\quad - \Big(y - \Big\lfloor \frac{N}{2} \Big\rfloor\Big)\Big(\Big(x - \Big\lfloor \frac{N}{2} \Big\rfloor\Big)^2 + \Big(y - \Big\lfloor \frac{N}{2} \Big\rfloor\Big)^2\Big), \end{aligned}$$

where $\rho_i \in \mathbb{R}$ and $\omega_i \in \mathbb{R}$ are parameters. Then, the two clocks C_i^X and C_i^Y trigger transitions of the discrete auxiliary variables P_i and Q_i as follows (see Fig. 4(a)).

If $C_i^X(t) = 1$, then

$$P_i(t_+) := \begin{cases} P_i(t) + 1 & \text{if } P_i(t) < |\mathcal{F}_i(X_i(t), Y_i(t))|, \\ 0 & \text{if } P_i(t) \ge |\mathcal{F}_i(X_i(t), Y_i(t))|, \end{cases} \tag{6}$$

If $C_i^Y(t) = 1$, then

$$Q_i(t_+) := \begin{cases} Q_i(t) + 1 & \text{if } Q_i(t) < |\mathcal{G}_i(X_i(t), Y_i(t))|, \\ 0 & \text{if } Q_i(t) \ge |\mathcal{G}_i(X_i(t), Y_i(t))|. \end{cases} \tag{7}$$

As a result, the dynamics of the CA oscillator are described by Eqs. (3), (4), (6), and (7), and characterized by the parameters

$$N, \; M, \; \rho_i, \; \omega_i, \; \alpha_i, \; T_i^X, \; T_i^Y. \tag{8}$$

Figs. 4 (b) and (c) show phase plane trajectories of the CA oscillator. The CA oscillator exhibits different behaviors, such as oscillation and convergence for different parameter values. The next subsection provides characterizations for such behaviors of the CA oscillator and describes the roles of the parameters.

B. ROLES OF PARAMETERS

We assume that the discrete state variable X_i is in a steady state for $t > T_s$. Then, the following is defined.

Definition 1 (Amplitude): The discrete state variable X_i is said to have an amplitude

$$r_i = \frac{X_i^{\max} - X_i^{\min}}{2},$$

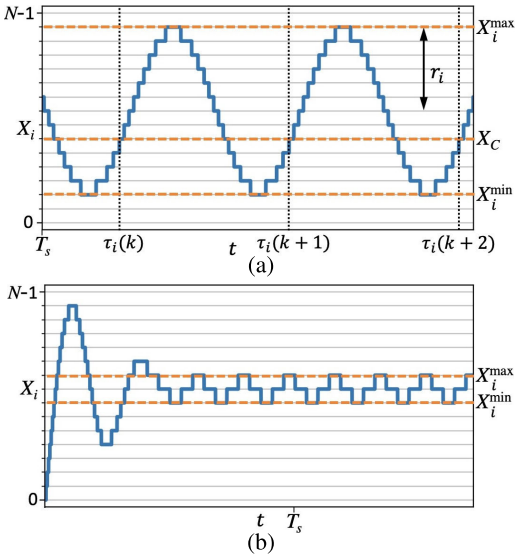

FIGURE 5. Definitions of the amplitude r_i and mean frequency f_i of the discrete state variable X_i. (a) Oscillation. The amplitude r_i is larger than the reference value $\lambda = 1$. (b) Convergence. The amplitude r_i is smaller than the reference value $\lambda = 1$.

TABLE 1. Roles of parameters.

Param.	Role
ρ_i	Adjustment of amplitude r_i of oscillation
ω_i	Adjustment of mean frequency f_i of oscillation
α_i	Scaling of mean frequency f_i of oscillation
T_i^X, T_i^Y	Adjustment of coexistence of multiple attractors
$w_{i,j}$	Adjustment of n:m phase-locking
	Adjustment of mean phase difference $\Phi_{i,j}$

where

$$\begin{aligned} X_i^{\max} &= \max\{X_i(t) \in \boldsymbol{Z}_N \mid t > T_s\}, \\ X_i^{\min} &= \min\{X_i(t) \in \boldsymbol{Z}_N \mid t > T_s\} \end{aligned}$$

are the maximum and minimum values of the discrete state variable X_i in the steady state, respectively.

For example, in Figs. 5(a) and (b), the amplitude r_i of the discrete state variable X_i is 6 and 1, respectively. Fig. 6 shows the characteristics of the amplitude r_i for the parameter ρ_i. Further, it shows the following relations between the parameter ρ_i and amplitude r_i.

- Fig. 6 shows that the amplitude r_i is approximately 0 for negative ρ_i and positive for positive ρ_i.
- Fig. 6 shows that the amplitude r_i is approximately proportional to $\sqrt{\rho_i}$ for relatively small positive ρ_i and saturates for large positive ρ_i.

The aforementioned relations reveal that the parameter ρ_i can adjust the amplitude r_i (see Table 1). Using the amplitude r_i, the following is defined.

Definition 2 (Oscillation and Convergent): The discrete state variable X_i is said to converge if $r_i \le \lambda$ and is said to oscillate if $r_i > \lambda$, where λ is an appropriately small positive constant, which is introduced to indicate that "the amplitude r_i is regarded to be almost 0 if $r_i \le \lambda$."

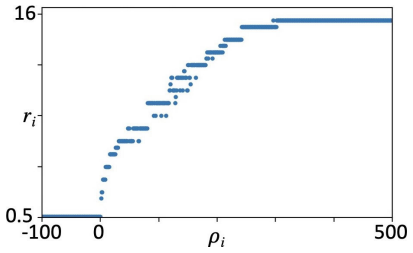

FIGURE 6. Characteristics of the amplitude r_i of the discrete state variable X_i for the parameter ρ_i. $N = 2^5$, $M = 2^6$, $\omega_i = 2\pi/\alpha_i$, $\alpha_i = 0.01$, $T_i^X = 0.0012236$, and $T_i^Y = 0.001$..

In this study, $\lambda = 1$ is chosen. In Fig. 5(a), the amplitude r_i is $5 > \lambda$; thus, the discrete state variable X_i oscillates. In Fig. 5(b), the amplitude r_i is $1 \leq \lambda$; thus, the discrete state variable X_i converges. Then, the following is defined.

Definition 3 (Mean Frequency): Assume the discrete state variable X_i oscillates and repeats to transit from a certain constant value $X_C - 1$ to X_C. Let $\tau_i(k)$ be the k-th moment when the discrete state variable X_i transits from the constant value $X_C - 1$ to X_C. Then, the discrete state variable X_i is said to have a mean frequency f_i defined by

$$f_i = \frac{K-1}{\sum_{k=1}^{K-1} \tau_i(k+1) - \tau_i(k)},$$

where K is an appropriately large positive integer. If the discrete state variable X_i converges, the mean frequency is defined as $f_i = 0$.

For example, in Figs. 5(a) and (b), the mean frequency f_i of the discrete state variable X_i is positive and 0, respectively. Fig. 7 shows the characteristics of the mean frequency f_i for the parameters ρ_i, ω_i, and α_i. These figures show the following roles of the parameters.

- Fig. 7(a) shows that the mean frequency f_i is almost constant with respect to the parameter $\rho_i > 0$.
- Figs. 7(b) and (c) show that the mean frequency f_i is almost proportional to the parameter ω_i.
- Figs. 7(b) and (c) show that the parameter α_i changes the scale of the mean frequency f_i.

The aforementioned relations show that the parameter ω_i can adjust the frequency f_i, while the parameter $\rho_i > 0$ does not affect the frequency r_i significantly (see Table 1). Further, the parameter α_i can scale the frequency f_i (see Table 1).

C. IMPORTANCE OF ASYNCHRONOUS TRANSITIONS

This subsection describes the importance of the asynchronous transitions of the discrete state variables X_i,Y_i, P_i, and Q_i.

Definition 4 (Asynchronous and Synchronous CA Oscillators): The CA oscillator is said to be

- *asynchronous CA oscillator if T_j^X/T_j^Y is irrational.*
- *synchronous CA oscillator if T_i^X/T_i^Y is rational.*[1]

[1]The synchronous CA oscillator for $T_i^X = T_i^Y$ (or the CA oscillator with a single clock with period T_i^X) has simultaneous transitions of the discrete state variables, and the synchronous CA oscillator for $T_i^X \neq T_i^Y$ has phase-locked transitions of the discrete state variables.

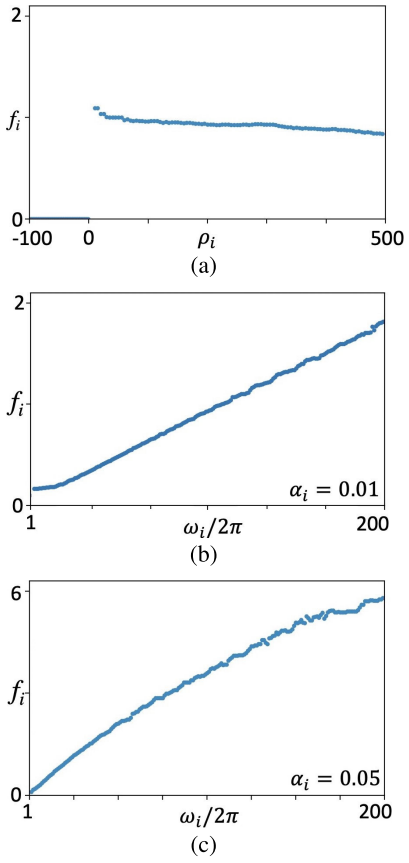

FIGURE 7. (a) Characteristics of the mean frequency f_i for the parameter ρ_i. $N = 2^5$, $M = 2^6$, $\omega_i = 2\pi/\alpha_i$, $\alpha_i = 0.01$, $T_i^X = 0.0012236$, and $T_i^Y = 0.001$. (b) Characteristics of the mean frequency f_i for the parameter ω_i. $N = 2^5$, $M = 2^6$, $\rho_i = 225$, $\alpha_i = 0.01$, $T_i^X = 0.0012236$, and $T_i^Y = 0.001$. (c) Characteristics of the mean frequency f_i for the parameter ω_i. $\alpha_i = 0.05$ and the remaining parameter values are equal to those in (b).

Then, we compare the characteristics of the asynchronous and synchronous CA oscillators.

(a) Fig. 8 shows the characteristics of the asynchronous CA oscillator. Fig. 8(a) shows an orbit of the discrete state vector (X_i, Y_i) in a steady state. Here, all the trajectories of the discrete state vector (X_i, Y_i) starting from different initial conditions are attracted into the same orbit in Fig. 8(a). For certain different parameter values, a small number of orbits coexist in steady states and the asynchronous CA oscillator exhibits one of them depending on the initial condition of the discrete state vector (X_i, Y_i). Fig. 8(b) shows the characteristics of the number of such coexisting orbits in steady states. The asynchronous CA oscillator has a single orbit in a steady state for a wide range of parameter values. Fig. 8(c) shows the characteristics of the maximum values $X_i^{\max}$ and minimum values $X_i^{\min}$ of the coexisting orbits.

(b) Fig. 9 shows the characteristics of the synchronous CA oscillator. Fig. 9(a) shows that the synchronous CA oscillator has many coexisting orbits and the oscillator exhibits one of orbits depending on the initial condition

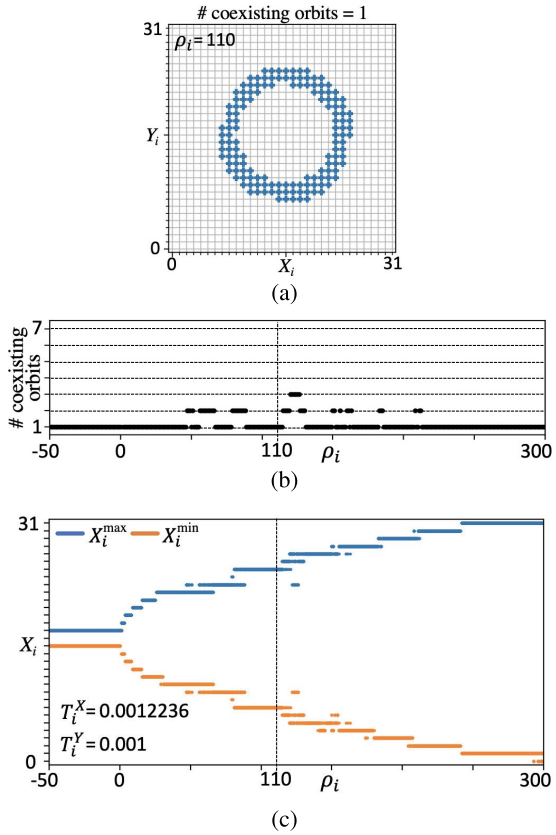

FIGURE 8. Characteristics of the asynchronous CA oscillator. $N = 2^5$, $M = 2^6$, $\omega_i = 2\pi/\alpha_i$, and $\alpha_i = 0.01$. $T_i^X = 0.0012236$ and $T_i^Y = 0.001$, where T_i^X/T_i^Y can be regarded as almost irrational. (a) Phase plain trajectories starting from the different initial conditions $X_i(0) \in Z_N$, $Y_i(0) = \lfloor N/2 \rfloor$, and $P_i(0) = Q_i(0) = 0$. $\rho_i = 110$. (b) Characteristics of the number of coexisting orbits. The vertical broken line corresponds to (a). (c) Characteristics of the maximum values X_i^{max} and minimum values X_i^{min} of the coexisting orbits. The vertical broken line corresponds to (a).

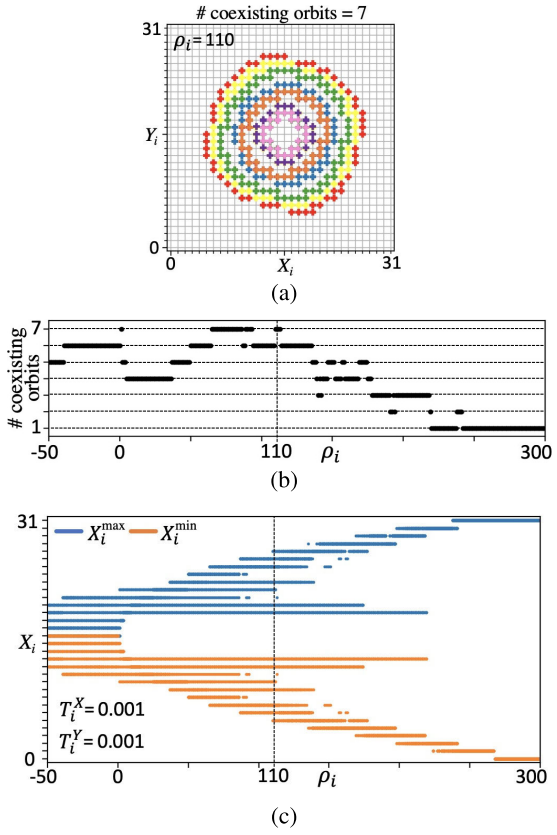

FIGURE 9. Characteristics of the synchronous CA oscillator. $N = 2^5$, $M = 2^6$, $\omega_i = 2\pi/\alpha_i$, and $\alpha_i = 0.01$. $T_i^X = 0.001$ and $T_i^Y = 0.001$, where T_i^X/T_i^Y is rational. (a) Phase plain trajectories starting from the different initial conditions $X_i(0) \in Z_N$, $Y_i(0) = \lfloor N/2 \rfloor$, and $P_i(0) = Q_i(0) = 0$. $\rho_i = 110$. (b) Characteristics of the number of coexisting orbits. The vertical broken line corresponds to (a). (c) Characteristics of the maximum values X_i^{max} and minimum values X_i^{min} of the coexisting orbits. The vertical broken line corresponds to (a).

of the discrete state vector (X_i, Y_i). Fig. 9(b) shows the characteristics of the number of such coexisting orbits, and Fig. 9(c) shows the characteristics of the maximum values $X_i^{\max}$ and minimum values $X_i^{\min}$ of the coexisting orbits. These figures show that the synchronous CA oscillator has multiple orbits in steady states for a wide range of parameter values.

The aforementioned characteristics show that the periods T_i^X and T_i^Y of the clocks C_i^X, and C_i^Y determine the characteristics of the coexisting orbits in steady states (see Table 1). Further, the aforementioned characteristics show the following significance of the analyses.

Remark 1 (Significance Obtained From the Analyses of Single Oscillator): The CA oscillator is used as an element of a CPG model in Section IV, where the amplitude r_i and mean frequency f_i of the discrete state variable X_i control an amplitude and a frequency of motion of a robot leg, respectively. In this context, the asynchronous CA oscillator is more suited to build the CPG model because the leg motion is expected to be controlled by the system parameters as a consequence of the analyses in Subsection II-B and characteristics (a) in Subsection II-C. If the synchronous CA oscillator is used to build the CPG model, the leg motion is not expected to be controlled by the system parameters as a consequence of the characteristics (b) in Subsection II-C. Using these analyses, a CPG model design is proposed in Section IV.

III. ANALYSES OF SMALL NETWORK OF CA OSCILLATORS AS PREPARATIONS TO DESIGN CPG

In this section, a small network of the CA oscillators is designed and analyzed to design the CPG model for controlling the hexapod robot in Fig. 1. The following is a procedure to design a modified CA oscillator to build the network.

A. MODIFIED CA OSCILLATOR FOR COUPLING

Fig. 10(a) shows a schematic diagram of the modified CA oscillator, where the dashed boxes represent modifications of the CA oscillator in Fig. 3. The modified CA oscillator has a clock

$$C_i^Z(t) = \sum_{k=0}^{\infty} \delta(t - kT_i^Z)$$

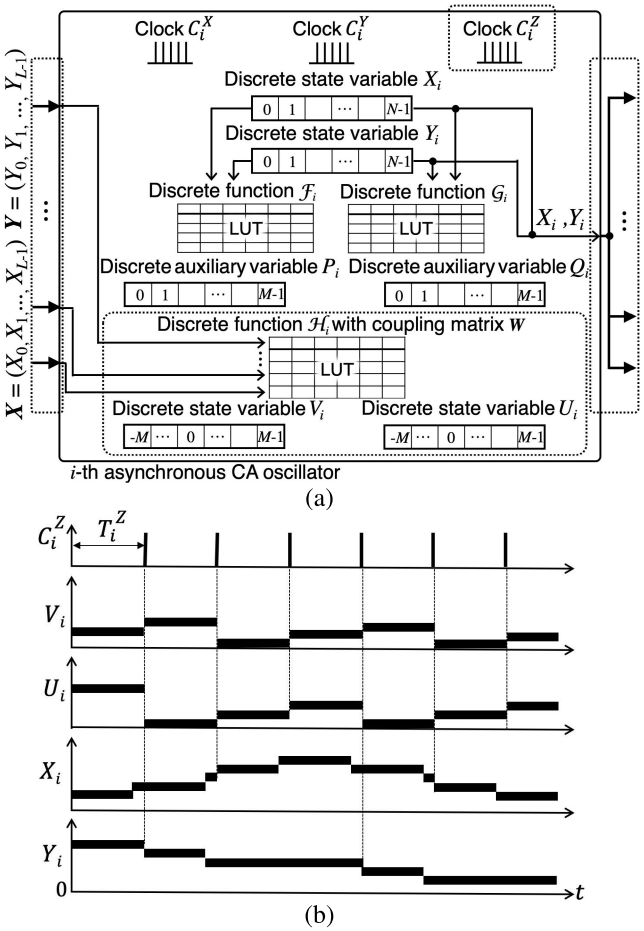

FIGURE 10. (a) Schematic diagram of the modified CA oscillator for coupling. (b) Timing chart of state transitions triggered by the clock C_i^Z.

for coupling, where $T_i^Z \in (0, \infty)$ is a clock period. Further, the modified CA oscillator has discrete state variables

$$V_i \in \boldsymbol{Z}_M, \quad U_i \in \boldsymbol{Z}_M \tag{9}$$

for coupling. The clock C_i^Z triggers transitions of the discrete state variables V_i and U_i as follows (see Fig. 10(b)).

$$\text{If } C_i^Z(t) = 1, \text{ then}$$
$$V_i(t_+) := \begin{cases} V_i(t)+1 & \text{if } V_i(t) < |\mathcal{H}_i(\boldsymbol{X}(t))|, \\ 0 & \text{if } V_i(t) \geq |\mathcal{H}_i(\boldsymbol{X}(t))|, \end{cases}$$
$$U_i(t_+) := \begin{cases} U_i(t)+1 & \text{if } U_i(t) < |\mathcal{H}_i(\boldsymbol{Y}(t))|, \\ 0 & \text{if } U_i(t) \geq |\mathcal{H}_i(\boldsymbol{Y}(t))|, \end{cases} \tag{10}$$

where $\boldsymbol{X}(t)$ and $\boldsymbol{Y}(t)$ denote vector forms

$$\boldsymbol{X}(t) = (X_0(t), X_1(t), \cdots, X_{L-1}(t)),$$
$$\boldsymbol{Y}(t) = (Y_0(t), Y_1(t), \cdots, Y_{L-1}(t)),$$

of the discrete state variables, L is the number of CA oscillators in the network, and $\mathcal{H}_i : \boldsymbol{Z}_N^L \to \boldsymbol{Z}_M^{\pm}$ denotes a discrete function

$$\mathcal{H}_i \equiv H_i \circ h_i, \tag{11}$$

which is implemented in a look-up-table, as shown in Fig. 10(a). In this study, we propose to design the function $H_i(\chi) : \mathbb{R} \to \boldsymbol{Z}_M^{\pm}$ as follows.

$$H_i(\chi) = \left\lfloor \frac{1}{\beta_i T_i^Z \chi} \right\rfloor,$$

where $\beta_i \in (0, \infty)$ is a scaling parameter and the function $H_i(\chi)$ is assumed to be saturated at $\pm(M-1)$. We further propose to design the function $h_i(\boldsymbol{\chi}) : \boldsymbol{Z}_N^L \to \mathbb{R}$ as follows.

$$h_i(\boldsymbol{\chi}) = \left\lfloor \sum_{j=0}^{L-1} w_{i,j} \left(\chi_j - \left\lfloor \frac{N}{2} \right\rfloor \right) \right\rfloor,$$

where $\boldsymbol{\chi} = (\chi_0, \chi_1, \cdots, \chi_{L-1})$ and the function $h_i(\boldsymbol{\chi})$ is assumed to be saturated at $\pm(M-1)$. In addition, $w_{i,j} \in \mathbb{R}$ represents a coupling strength from the j-th CA oscillator to the i-th CA oscillator and forms a matrix form

$$\boldsymbol{W} = \begin{pmatrix} w_{0,0} & \cdots & w_{0,L-1} \\ \vdots & \ddots & \vdots \\ w_{L-1,0} & \cdots & w_{L-1,L-1} \end{pmatrix}.$$

Then, the clock C_i^Z triggers transitions of the discrete state variables X_i and Y_i as follows (see also Fig. 10(b)).

$$\text{If } C_i^Z(t) = 1 \text{ and } V_i(t) \geq |\mathcal{H}_i(\boldsymbol{X}(t))|, \text{ then}$$
$$X_i(t_+) := \begin{cases} X_i(t)+1 & \text{if } \mathcal{H}_i(\boldsymbol{X}(t)) \geq 0 \text{ and } X_i(t) < N-1, \\ X_i(t)-1 & \text{if } \mathcal{H}_i(\boldsymbol{X}(t)) < 0 \text{ and } X_i(t) > 0. \end{cases} \tag{12}$$

$$\text{If } C_i^Z(t) = 1 \text{ and } U_i(t) \geq |\mathcal{H}_i(\boldsymbol{Y}(t))|, \text{ then}$$
$$Y_i(t_+) := \begin{cases} Y_i(t)+1 & \text{if } \mathcal{H}_i(\boldsymbol{Y}(t)) \geq 0 \text{ and } Y_i(t) < N-1, \\ Y_i(t)-1 & \text{if } \mathcal{H}_i(\boldsymbol{Y}(t)) < 0 \text{ and } Y_i(t) > 0. \end{cases} \tag{13}$$

Therefore, the dynamics of the modified CA oscillator are described by Eqs. (10), (12), and (13) in addition to Eqs. (3), (4), (6), and (7) and have the parameters

$$\beta_i, \ T_i^Z, \ w_{i,0}, \cdots, w_{i,L} \tag{14}$$

in addition to the parameters in Eq. (8).

B. ANALYSES OF SMALL NETWORK AS PREPARATIONS TO DESIGN CPG

We analyze a network of two CA oscillators in Fig. 11(a), which has a matrix form

$$\boldsymbol{W} = \begin{pmatrix} 0 & w_{0,1} \\ w_{1,0} & 0 \end{pmatrix}$$

of the coupling strength $w_{i,j}$. Figs. 11(b) and (c) show the time waveforms of the discrete state variables (X_i, Y_i) of the network for different parameter values. To characterize such waveforms, we introduce a phase $\phi_i(t)$ and restricted phase $\hat{\phi}_i(t)$ of the state vector $(X_i(t), Y_i(t))$ as follows.

$$\phi_i(t) = \mathrm{Arg}\left(\left(X_i(t) - \left\lfloor \frac{N}{2} \right\rfloor \right) + \mathrm{j} \left(Y_i(t) - \left\lfloor \frac{N}{2} \right\rfloor \right) \right),$$

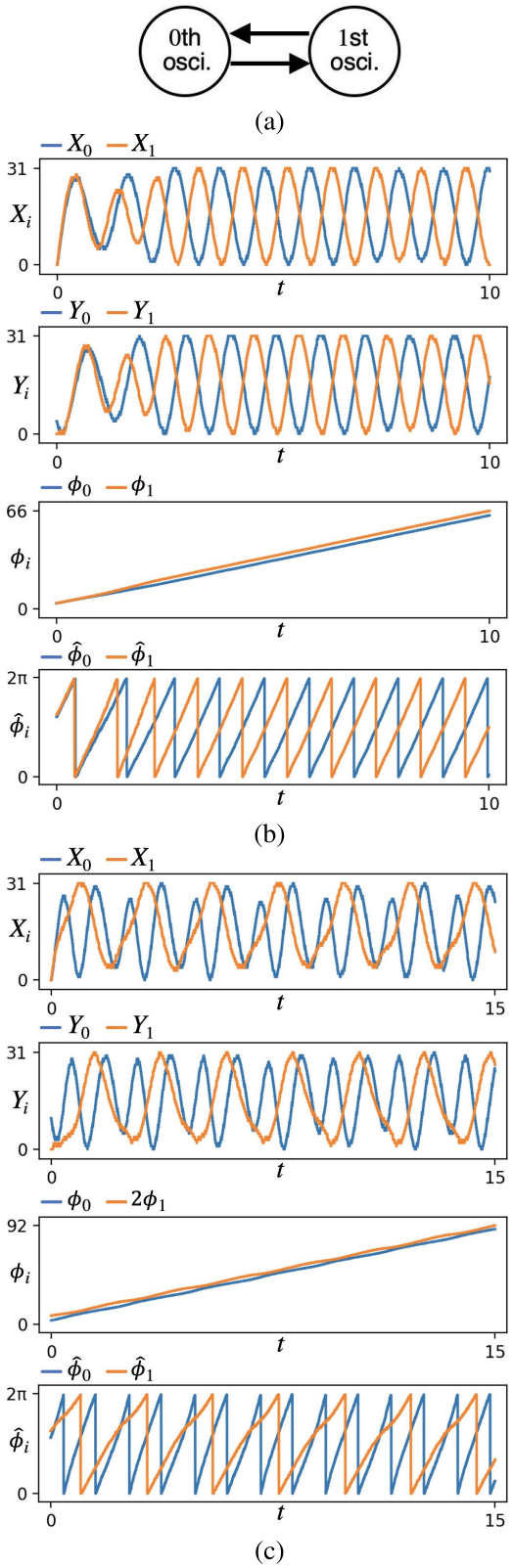

FIGURE 11. (a) Network of $L = 2$ CA oscillators. $N = 2^5$, $M = 2^6$, $\rho_0 = \rho_1 = 200$, $\alpha_0 = \alpha_1 = 0.01$, $T_0^X = T_1^Y = 0.0012236$, $T_0^Y = T_1^Y = 0.001$, $\beta_0 = \beta_1 = 1$, and $T_0^Z = T_1^Z = 0.01$. (b) 1:1 phase-locking. $\omega_0 = \omega_1 = 2\pi/\alpha$ and $w_{0,1} = w_{1,0} = -1$. The mean phase difference is $\Phi_{0,1} = -3.14$. (c) 1:2 phase-locking. $\omega_0 = 2\pi/\alpha$, $\omega_1 = 0.4 \times \omega_0$, $w_{1,2} = w_{2,1} = -1.1$. The mean phase difference is $\Phi_{0,1} = -2.87$.

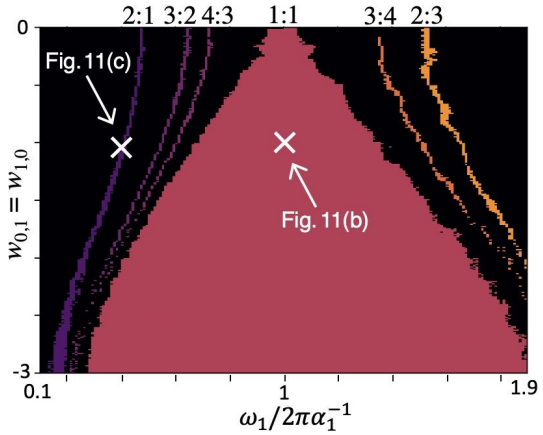

FIGURE 12. Parameter regions where *n:m* phase-lockings are observed. $L = 6$, $N = 2^5$, $M = 2^6$, $\rho_0 = \rho_1 = 200$, $\omega_0 = 2\pi/\alpha_0$, $\alpha_0 = \alpha_1 = 0.01$, $T_X^{(0)} = T_X^{(1)} = 0.0012236$, $T_Y^{(0)} = T_Y^{(1)} = 0.001$, $\beta_0 = \beta_1 = 1$, and $T_Z^{(0)} = T_Z^{(1)} = 0.01$.

$$\hat{\phi}_i(t) = \phi_i(t) + 2\pi\Omega,$$

where

$$\mathrm{Arg}(x + \mathrm{j}y) = \begin{cases} \arctan(y/x) + \pi & \text{if } x < 0, \\ \arctan(y/x) & \text{if } x > 0 \text{ and } y \geq 0, \\ \arctan(y/x) + 2\pi & \text{if } x > 0 \text{ and } y < 0, \\ \pi/2 & \text{if } x = 0 \text{ and } y > 0, \\ 3\pi/2 & \text{if } x = 0 \text{ and } y < 0, \end{cases}$$

which is undefined if $\sqrt{x^2 + y^2} \leq \kappa$ and κ are introduced to indicate that "the radius of (x, y) is regarded to be almost zero if $\sqrt{x^2 + y^2} \leq \kappa$." Further, Ω denotes "the number of times the state vector $(X_i(t), Y_i(t))$ has passed through a subset

$$\mathbf{\Gamma} \equiv \left\{ \left(x, y\right) \in \mathbf{Z}_N^2 \;\middle|\; x > \left\lfloor \frac{N}{2} \right\rfloor, y = \left\lfloor \frac{N}{2} \right\rfloor \right\}$$

of the state space counterclockwise." Figs. 11(b) and (c) show the time waveforms of the phases $(\phi_0(t), \phi_1(t))$ and restricted phases $(\hat{\phi}_0(t), \hat{\phi}_1(t))$ corresponding to the time waveforms of the discrete state variables $(X_i(t), Y_i(t))$. Using the phase $\phi_i(t)$, the following is defined.

Definition 5 (Phase-Locking): The i-th and j-th CA oscillators are said to exhibit n:m phase-locking if there exists positive constants k and T_p, and coprime integers n and m such that

$$|n\phi_i(t) - m\phi_j(t)| < k \quad \text{for} \quad t > T_p.$$

For example, in Figs. 11 (b) and (c), the CA oscillator exhibits 1:1 and 1:2 phase-lockings, respectively. Fig. 12 shows the parameter regions where various *n:m* phase-lockings are observed. The figure shows that the coupling strength $w_{i,j}$ can adjust the *n:m* phase-locking (see Table 1). Then, the following is defined.

Definition 6 (Mean Phase Difference): Assume the i-th and j-th CA oscillators exhibit n:m phase-locking. Then, the i-th CA oscillator is said to have a mean phase difference

$$\Phi_{i,j} = \frac{1}{T - T_p} \int_{T_p}^{T} n\phi_i(t) - m\phi_j(t)\, dt$$

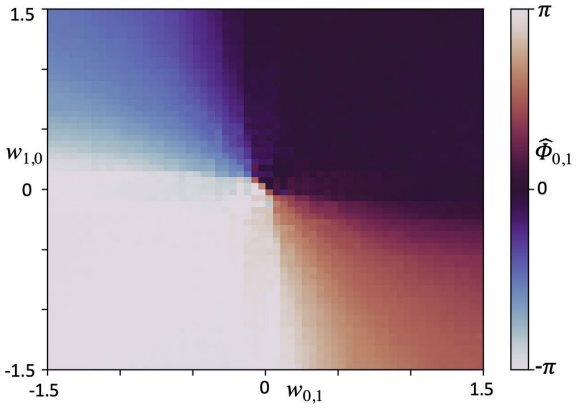

FIGURE 13. Characteristics of mean phase difference $\Phi_{i,j}$ of the network of the two CA oscillators in Fig. 11(a). $L = 6$, $N = 2^5$, $M = 2^6$, $\rho_0 = \rho_1 = 200$, $\omega_0 = 2\pi/\alpha_0$, $\omega_1 = 2\pi/\alpha_1$, $\alpha_0 = \alpha_1 = 0.01$, $T_X^{(0)} = T_X^{(1)} = 0.0012236$, $T_Y^{(0)} = T_Y^{(1)} = 0.001$, $\beta_0 = \beta_1 = 2$, and $T_Z^{(0)} = T_Z^{(1)} = 0.01$.

with respect to the j-th CA oscillator, where T is an appropriately large number.

For example, in Figs. 11 (b) and (c), the 0-th CA oscillator has mean phase differences $\Phi_{0,1} = -3.14$ and -2.87 with respect to the 1st CA oscillator, respectively. Fig. 13 shows the characteristics of the mean phase difference $\Phi_{0,1}$ for the coupling strengths $w_{0,1}$ and $w_{1,0}$. The figure shows that the coupling strength $w_{i,j}$ can adjust the mean phase difference $\Phi_{i,j}$ (see Table 1).

Remark 2 (Significance Obtained From the Analyses Of Small Network): A network of the CA oscillators is used as the CPG model in Section IV, where the ratio $n : m$ and mean phase difference $\Phi_{i,j}$ of phase locking determine a spatiotemporal pattern of the orbits of the legs of the robot. Here, the analysis results of the $n : m$ phase locking in Fig. 12 and that of the mean phase difference $\Phi_{i,j}$ in Fig. 13 are expected to be useful to design the CPG model. The significances of the analysis results in the CPG design are described in Section IV.

IV. DESIGN OF CPG CONSISTING OF NETWORK OF CA OSCILLATORS

Using the analyses of the single CA oscillator in Section II and those of the small network of the CA oscillators in Section III, in this section, we propose systematic design procedures of a network of the CA oscillators to control the hexapod robot in Fig. 1. Here, we introduce a bio-inspired target pattern of phase-lockings.

A. TARGET PHASE-LOCKING PATTERN FOR CONTROLLING HEXAPOD ROBOT

Fig. 14(a) shows an illustration of an insect, where its six legs are labeled as 0–5. Fig. 14(b) shows a timing chart of a gait, where the horizontal axis represents the time and vertical axis represents movement of each leg relative to the ground. In this chart, the black bar shows the moment when the leg is off the ground and moving forward, and the white region indicates

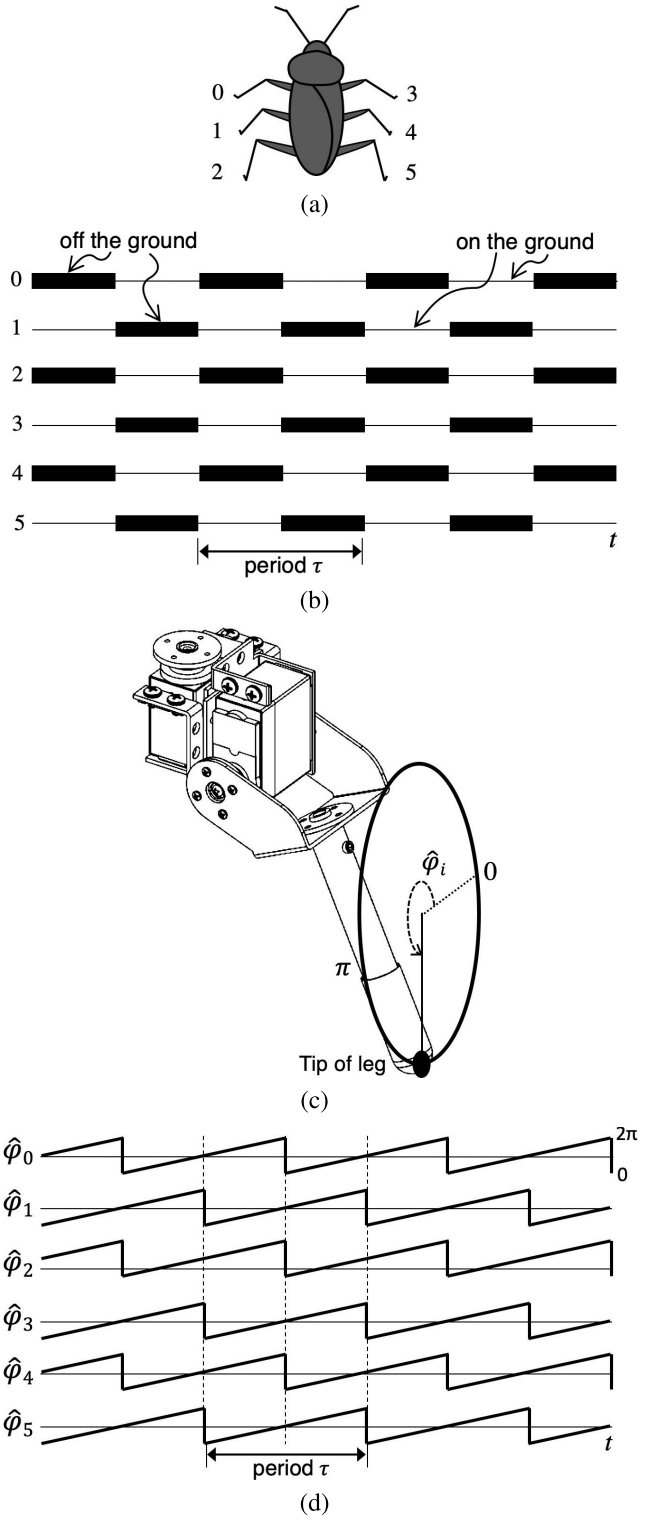

FIGURE 14. (a) Illustration of a six-legged insect. (b) Timing chart of a tripod gait [37]. (c) i-th leg of the hexapod robot in Fig. 1. The orbit of the tip of the leg is represented by the angle $\hat{\varphi}_i$. (d) Example of pattern of time-dependent angles $\hat{\varphi}_0(t), \cdots, \hat{\varphi}_5(t)$. This pattern is used as a target phase-locking pattern of the CPG.

the moment when the leg is touching and crawling on the ground. The gait in Fig. 14(b) is called a tripod gait, which is one of the typical gaits of six-legged insects [37]. As shown in

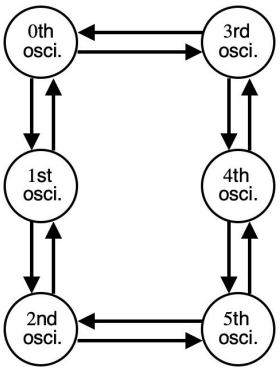

FIGURE 15. Network of six CA oscillators used as a CPG to control the hexapod robot in Fig. 1.

the figure, a pair of black bar and white region form a period τ of the tripod gait. Fig. 14(c) shows the i-th leg of the hexapod robot in Fig. 1. The orbit of the tip of the leg is represented by an angle $\hat{\varphi}_i \in [0, 2\pi)$. We consider a time-varying angle

$$\hat{\varphi}_i(t) = \frac{2\pi}{\tau}t + \gamma_i \ (\mathrm{mod}\ 2\pi),$$

where $\gamma_i \in [0, 2\pi)$ is an offset parameter. Fig. 14(d) shows an example of the pattern of six time-varying angles $(\hat{\varphi}_0(t), \cdots, \hat{\varphi}_5(t))$. Further, we consider a map

$$\sigma(\hat{\varphi}_i) = \begin{cases} \text{“black bar”} & \text{if } \hat{\varphi}_i \geq \pi, \\ \text{“white region”} & \text{if } \hat{\varphi}_i < \pi. \end{cases}$$

Applying the map σ to the six time-varying angles$(\hat{\varphi}_0(t), \cdots, \hat{\varphi}_5(t))$ in Fig. 14(d), the gait diagram in Fig. 14(b) is obtained. Hence, here, six CA oscillators are constructed to reproduce the time-varying angles $(\hat{\varphi}_0(t), \cdots, \hat{\varphi}_5(t))$ in Fig. 14(d). They are expected to exhibit the following pattern of phase-lockings.

Target phase-locking pattern of six CA oscillators:

(i) *Each pair of CA oscillators exhibits* 1:1 *phase-locking.*
(ii) *Each mean phase difference* $\Phi_{i,j}$ *for* $i \in \{0, 2, 4\}$ *and* $j \in \{0, 2, 4\}$ *is almost zero.*
(iii) *Each mean phase difference* $\Phi_{i,j}$ *for* $i \in \{1, 3, 5\}$ *and* $j \in \{1, 3, 5\}$ *is almost zero.*
(iv) *Each mean phase difference* $\Phi_{i,j}$ *for* $i \in \{0, 2, 4\}$ *and* $j \in \{1, 3, 5\}$ *is almost* π.
(v) *Each mean phase difference* $\Phi_{i,j}$ *for* $i \in \{1, 3, 5\}$ *and* $j \in \{0, 2, 4\}$ *is almost* π.

The next subsection proposes the systematic design procedures of a network of the CA oscillators, which is used as a CPG to generate the aforementioned target phase-locking pattern.

B. DESIGN OF NETWORK OF CA OSCILLATORS USED AS CPG TO GENERATE TARGET PHASE-LOCKING

We propose to use the network of the CA oscillators in Fig. 15 as a CPG to generate the target phase-locking pattern. The parameters are designed as follows.

Design Procedure 1 (Parameters): The parameter vector $(\rho_i, \omega_i, \alpha_i, \beta_i, T_i^Z)$ *of each modified CA oscillator is set to have the same value, and the coupling strengths* $w_{i,j}$ *among the oscillators are set to*

$$\boldsymbol{W} = \begin{pmatrix} 0 & -1 & 0 & -1 & 0 & 0 \\ -1 & 0 & -1 & 0 & 0 & 0 \\ 0 & -1 & 0 & 0 & 0 & -1 \\ -1 & 0 & 0 & 0 & -1 & 0 \\ 0 & 0 & 0 & -1 & 0 & -1 \\ 0 & 0 & -1 & 0 & -1 & 0 \end{pmatrix}. \tag{15}$$

Further, the values of the parameters ρ_i *and* (ω_i, α_i) *are adjusted to realize the desired amplitude and frequency of the motion of the hexapod robot leg.*

Here, the significances of the analyses in Section III explained in Remark 2 are as follows.

- Fig. 12 shows that a pair of the i-th and j-th CA oscillators with the same value of the parameter vector $(\rho_i, \omega_i, \alpha_i, \beta_i, T_i^Z)$ and coupled via the strengths $w_{i,j} = w_{j,i} = -1$ exhibits a 1:1 phase-locking. Hence, the design procedure 1 is considered suitable to realize the item (i) of the target phase-locking pattern.
- Fig. 13 shows that a pair of the i-th and j-th CA oscillators with the same value of the parameter vector $(\rho_i, \omega_i, \alpha_i, \beta_i, T_i^Z)$ coupled via the strengths $w_{i,j} = w_{j,i} = -1$ demonstrate mean phase differences $|\Phi_{i,j}| \simeq |\Phi_{j,i}| \simeq \pi$. Then, the network topology in Fig. 15 is considered suitable to realize the items (ii)–(v) of the target phase-locking pattern.

However, the design procedure 1 is not sufficient. Recall that the Remark 1 in Section II shows that the ratio of the clock periods of the CA oscillator should be tuned to design a CPG model, e.g., an irrational ratio of the clock periods and resulting asynchronous state transitions are preferred. Then, to characterize the networks of the CA oscillators with various ratios of the clock periods, the following is defined.

Definition 7 (Asynchronous and Synchronous Networks): The network of the CA oscillators is said to be

- *asynchronous network if* T_i^X/T_j^X *and/or* T_i^Y/T_j^Y *is irrational for certain* $i \neq j$.
- *synchronous network if* T_i^X/T_j^X *and* T_i^Y/T_j^Y *are rational for all* i *and* j.

Then, the following four types of networks exist.
(a) *Asynchronous network of Asynchronous CA oscillators.*
(b) *Synchronous network of Asynchronous CA oscillators.*
(c) *Asynchronous network of Synchronous CA oscillators.*
(d) *Synchronous network of Synchronous CA oscillators.*

We compare the characteristics of these networks and their relations with the target phase-locking pattern, where the aforementioned (a)–(d) correspond to the following (a)–(d), respectively.

(a) Fig. 16(a) shows the time waveforms of the discrete state variables (X_i, Y_i) and corresponding restricted phase $\hat{\phi}_i$ of an *asynchronous network of asynchronous CA oscillators*. Each restricted phase $\hat{\phi}_i$ is not defined for $t < p_i^a$

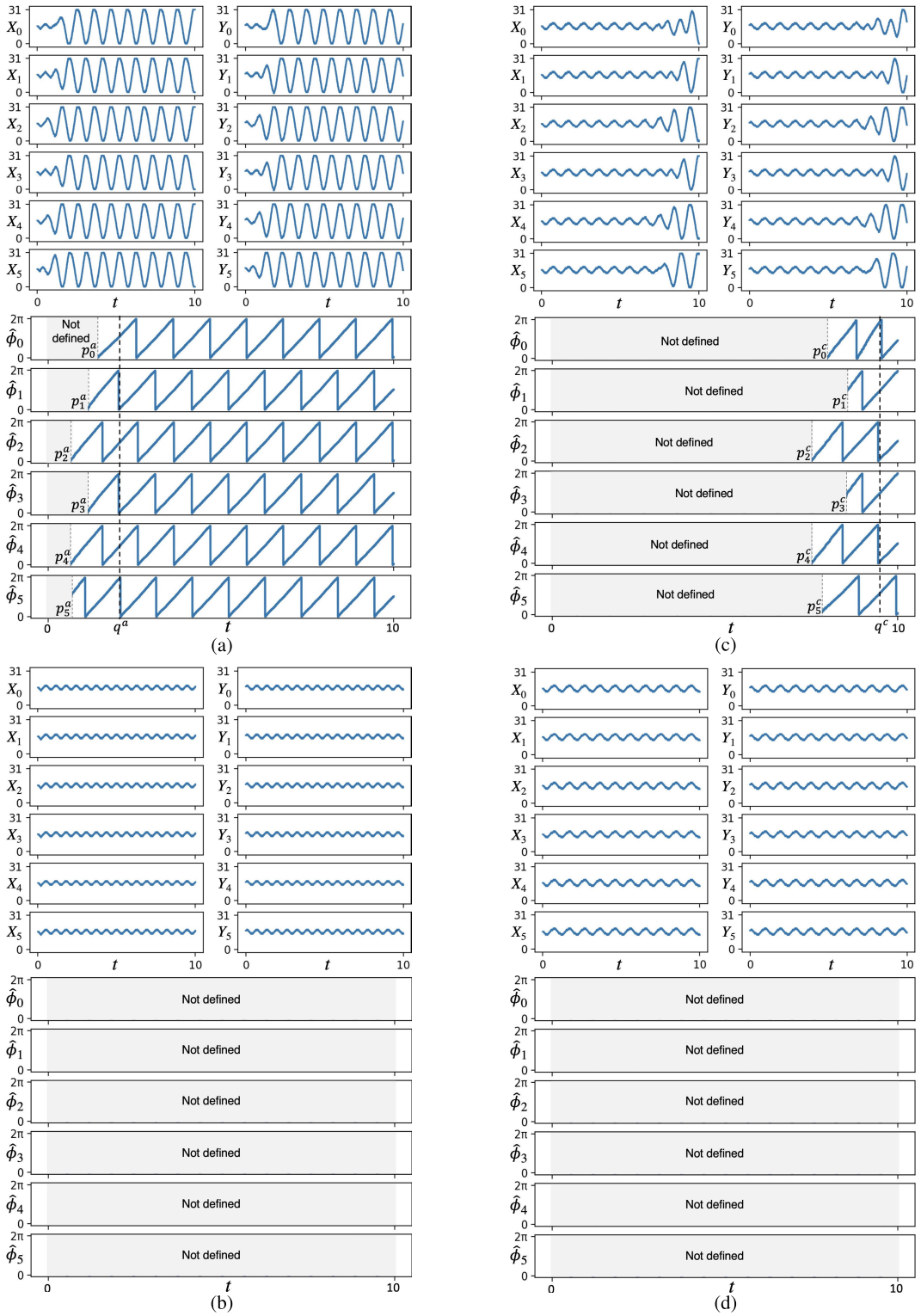

FIGURE 16. Time waveforms of the discrete state variables (X_i, Y_i) and corresponding restricted phases $\hat{\phi}_i$ of four networks of CA oscillators. $L = 6$, $N = 2^5$, $M = 2^6$, $\rho_i = 200$, $\omega_i = 2\pi/\alpha_i$, $\alpha_i = 0.01$, $\beta_i = 1$, and $T_i^Z = 0.01$ for all i. $(X_i(0), Y_i(0), P_i(0), Q_i(0), V_i(0), U_i(0)) = (16, 17, 0, 0, 0, 0)$ for all i. $\kappa = 3$. (a) Asynchronous network of Asynchronous CA oscillators. $T_i^X = 0.00100031415$ and $T_i^Y = 0.001$ for $i = 0, 1, 2, 3$, and 4. $T_5^X = 0.001$ and $T_5^Y = 0.00100031415$. (b) Synchronous network of Asynchronous CA oscillators. $T_i^X = 0.00100031415$ and $T_i^Y = 0.001$ for all i. (c) Asynchronous network of Synchronous CA oscillators. $T_i^X = T_i^Y = 0.001$ for $i = 0, 1, 2, 3$, and 4. $T_5^X = T_5^Y = 0.00100031415$. (d) Synchronous network of Synchronous CA oscillators. $T_i^X = T_i^Y = 0.001$ for all i. The ratio 0.00100031415/0.001 is regarded as an irrational number owing to the C language implementation of real numbers.

TABLE 2. Comparison of four networks.

	Asynchronous network of asynchronous CA osci.	Synchronous network of asynchronous CA osci.	Asynchronous network of synchronous CA osci.	Synchronous network of synchronous CA osci.
Waveforms	Fig. 16(a)	Fig. 16(b)	Fig. 16(c)	Fig. 16(d)
Restricted phase $\hat{\phi}_i$	Defined	Not defined (too small amplitude)	Defined	Not defined (too small amplitude)
Realization of target phase-locking	Yes	No	Yes	No
Transient to target phase-locking	Short	-	Long	-
Suitability to be used as CPG	Suited	Not suited	Not suited (too long transient)	Not suited

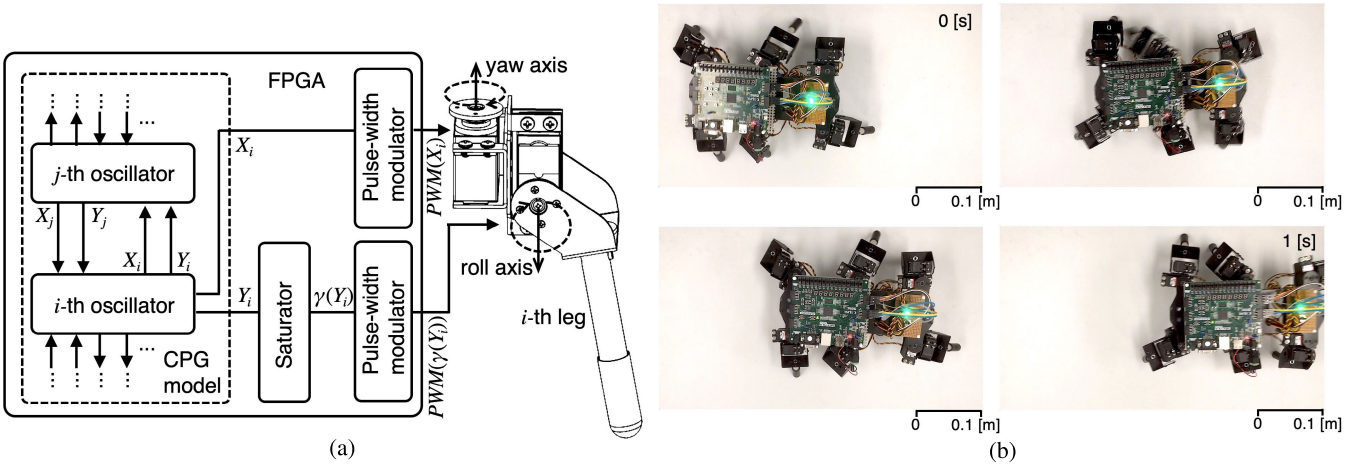

FIGURE 17. (a) Structure of each leg. Each leg has Hitec's servomotors HS-422 (yaw axis) and HS-645MG (roll axis). (b) Tripod gait of the robot. $N = 2^5$, $M = 2^6$, $\rho_i = 200$, $\omega_i = 2\pi/\alpha_i$, $\alpha_i = 0.01$, $L = 6$, $\beta_i = 1$, and $T_i^Z = 0.01$ for all i. $T_i^X = 0.0012236$ and $T_i^Y = 0.001$ for $i = 0, 1, 2, 3$, and 4. $T_5^X = 0.001$ and $T_5^Y = 0.0012236$.

as the radius $\sqrt{(X_i - \lfloor N/2 \rfloor)^2 + (Y_i - \lfloor N/2 \rfloor)^2}$ is too small (i.e., smaller than κ). Further, the network exhibits the target phase-locking pattern for $t > q^a$ (see Table 2).

(b) Fig. 16(b) shows the time waveforms of a *synchronous network of asynchronous CA oscillators*. Each restricted phase $\hat{\phi}_i$ is not defined for $t > 0$ as the radius $\sqrt{(X_i - \lfloor N/2 \rfloor)^2 + (Y_i - \lfloor N/2 \rfloor)^2}$ is too small. Hence, the synchronous network of the asynchronous CA oscillators cannot realize the target phase-locking pattern (see Table 2).

(c) Fig. 16(c) shows the time waveforms of an *asynchronous network of the synchronous CA oscillators*. The time interval $[0, p_i^c)$ where each restricted phase $\hat{\phi}_i$ is not defined is much longer than that of the asynchronous network of the asynchronous CA oscillators. The transient time interval $[0, q^c)$ to achieve the target synchronization is much longer than that of the asynchronous network of the asynchronous CA oscillators. Hence, the asynchronous network of the synchronous CA oscillators is not suitable to be used as a CPG when compared with the asynchronous network of the asynchronous CA oscillators (see Table 2).

(d) Fig. 16(d) shows the time waveforms of a *synchronous network of the synchronous CA oscillators*. The figure shows that each restricted phase $\hat{\phi}_i$ is not defined for $t > 0$ as the radius $\sqrt{(X_i - \lfloor N/2 \rfloor)^2 + (Y_i - \lfloor N/2 \rfloor)^2}$ is too small. Hence, the synchronous network of asynchronous CA oscillators cannot realize the target phase-locking pattern (see Table 2).

The aforementioned four characteristics reveal the following consequence.

Remark 3 (Significance Obtained From Analyses of CPG Network): The asynchronous network of asynchronous CA oscillators is best suitable to be used as the CPG as summarized in Table 2.

Thus, we propose the following design procedure.

Design Procedure 2 (Asynchronous Clocks): Each CA oscillator is set to have the clocks C_i^X and C_i^Y that have an irrational ratio T_i^X/T_i^Y of the periods. Further, at least one pair of the CA oscillators in the network is set to have an irrational ratio T_i^X/T_j^X or T_i^Y/T_j^Y of the periods of the clocks.

Using the design procedures 1 and 2, the asynchronous network of the asynchronous CA oscillators can be designed, which can realize the target phase-locking pattern with a short transient period, as shown in Fig. 16(a).

V. IMPLEMENTATION AND COMPARISON

A. IMPLEMENTATION

This subsection shows that the proposed CPG model designed by the procedures proposed in the previous section can

TABLE 3. Comparisons.

	Proposed CPG model implemented by asynchronous sequential logic	**Hopf CPG model** [3] **implemented by customized hardware DSP**	**Proposed CPG model implemented as software running on customized CPU**	**Previous CPG model** [33] **implemented by asynchronous sequential logic**
Bit length	$n = 5$ bit, $m = 6$ bit	14-bit fixed point	32-bit integer	$n = 5$ bit, $m = 10$ bit
Number of slices	892	3079	1458	1113
Number of LUTs	3192	9763	3548	3816
Number of FFs	497	370	3535	652
Number of BRAMs	-	-	52	-
On-Chip Power	0.218 W	0.421 W	0.313 W	0.248 W
Oscillation frequency determining gate velocity	1 Hz	1 Hz	1 Hz	1 Hz

Notes: LUT represents look-up-table, FF represents flip-flop, and BRAM represents block random access memory. For comparison, each model is implemented by the same design software environment and same FPGA device used to implement the proposed model. Each on-chip power is estimated by the same method used to estimate the power of the proposed model.

realize the tripod gait of the hexapod robot in Fig. 1. The dynamics of the CA oscillator are described as a register transfer level (RTL) VHDL code as follows. The discrete state variables (X_i, Y_i) are described by unsigned integers to reflect Eq. (1) and implemented by n-bit registers, where $n = \lceil \log_2 N \rceil$. The discrete auxiliary variables (P_i, Q_i) are described by unsigned integers to reflect Eq. (2) and implemented by m-bit registers, where $m = \lceil \log_2 M \rceil$. The functions $\mathcal{F}_i$ and $\mathcal{G}_i$ are described by two's compliment signed integers to reflect Eq. (5) and implemented by look-up-tables with n-bit unsigned inputs and an $(m + 1)$-bit signed output. Then, the state transitions in Eqs. (3), (4), (6), and (7) are described by sequential statements triggered by the clocks C_i^X and C_i^Y. Using the aforementioned CA oscillator as a component, the dynamics of the proposed CPG model are described as an RTL VHDL code as follows. The discrete state variables (V_i, U_i) for the coupling are represented by unsigned integers to reflect Eq. (9) and implemented by m-bit registers. The function $\mathcal{H}_i$ for the coupling is represented by two's compliment signed integers to reflect Eq. (11) and implemented by adders and look-up-tables with an $(n+1)$-bit signed input and $(m + 1)$-bit signed output. The state transitions in Eqs. (10), (12), and (13) realize the coupling of the asynchronous CA oscillators. Then, these state transitions are described by sequential statements triggered by the clock C_i^Z. Fig. 17(a) shows a structure of the hexapod robot leg. The discrete state variable X_i of the i-th CA oscillator is transformed into a pulse-width modulated (PWM) signal $PWM(X_i)$ by a pulse-width modulator, PWM signal $PWM(X_i)$ instructs the angle of the servomotor, and then, the servomotor determines the angle in the yaw axis of the i-th leg of the hexapod robot. Further, the discrete state variable Y_i of the i-th CA oscillator is transformed into a saturated signal $\gamma(Y_i)$ by a saturator

$$\gamma(Y_i) = \begin{cases} Y_i & \text{if } Y_i \geq N/2, \\ 0 & \text{otherwise}, \end{cases} \tag{16}$$

the saturated signal $\gamma(Y_i)$ is transformed into a PWM signal $PWM(\gamma(Y_i))$ by the pulse-width modulator, the PWM signal $PWM(\gamma(Y_i))$ instructs the angle of the servomotor, and then, the servomotor determines the angle in the roll axis of the i-th leg. The set of VHDL codes describing the CPG model, pulse-width modulators, and saturators are compiled by Xilinx's design software environment Vivado 2018.2 and a resulting bitstream file is downloaded to Xilinx's FPGA Artix-7 XC7A100T-1CSG324C [39] mounted on Digilent's Nexys 4 DDR evaluation platform [40]. Because the FPGA and design software environment used in this study do not support asynchronous triggering, the clocks C_i^X, C_i^Y, and C_i^Z are generated from a common clock with a high frequency (100[MHz]) such that the least common multiple of the periods of the clocks is much longer than the periods of oscillations of the discrete state variables X_i and Y_i. Thus, the clocks can be regarded to be asynchronous in practice. Fig. 17(b) shows snapshots of the hexapod robot controlled by the proposed CPG model. It can be observed that the robot can realize the tripod gait. Features of the proposed CPG model implemented by FPGA are summarized in Table 3. The bit lengths n and m are sufficiently shortened under the condition that the hexapod robot realizes an appropriate tripod gait, where the resulting bit lengths are $n = 5$ and $m = 6$. The on-chip power is the total of static power consumption (e.g., device static power) and dynamic power consumption (e.g., powers of clock, signal, logic, and BRAM). It is estimated by the design software environment at the post-routing stage, which provides the most accurate power estimation when compared with other design stages, such as post-synthesize and post-implementation stages.

B. COMPARISONS

This subsection compares the proposed CPG model with other CPG models.

1) HOPF CPG MODEL IMPLEMENTED BY CUSTOMIZED DSP

For comparison, we introduce the following Hopf CPG model as a conventional model [3].

$$\begin{aligned} x_i(t+h) &= x_i(t) + h(F_x(x_i(t), y_i(t)) + \sum_{j=0}^{5} w_{i,j}x_j(t)), \\ y_i(t+h) &= y_i(t) + h(F_y(x_i(t), y_i(t)) + \sum_{j=0}^{5} w_{i,j}y_j(t)), \\ F_x(x_i, y_i) &= (\mu_i^2 - (x_i^2 + y_i^2))x_i - \xi_i y_i, \\ F_y(x_i, y_i) &= (\mu_i^2 - (x_i^2 + y_i^2))y_i + \xi_i x_i, \end{aligned} \tag{17}$$

where h is a stepsize of the time t, $x_i \in \mathbb{R}$ and $y_i \in \mathbb{R}$ are continuous state variables, and $w_{i,j}$ is the coupling strength defined in Eq. (15). Further, $\mu_i \in \mathbb{R}$ and $\xi_i \in \mathbb{R}$ are parameters characterizing an amplitude and intrinsic oscillation frequency of the state variables (x_i, y_i), respectively. Fig. 18 shows time waveforms of the Hopf CPG model. It can be observed that the Hopf CPG model realizes the target phase-locking pattern. The dynamics of the Hopf CPG model in Eq. (17) are described as an RTL VHDL code as follows. The discrete state variables (x_i, y_i) and parameters (μ_i, ξ_i) are described by signed fixed point numbers with 8-bit integer parts and 5-bit decimal parts, and implemented by 14-bit registers. The coupling terms are described by summations and implemented by adders. Then, the state transitions in Eq. (17) are described by sequential statements that are triggered by a single clock. The state variable x_i is transformed into a PWM signal $PWM(ax_i + b)$ by the pulse-width modulator to determine the angle of the yaw axis of the i-th leg of the hexapod robot. Further, the state variable y_i is transformed into a saturated signal $\gamma(ay_i + b)$ by the saturator, and the saturated signal $\gamma(ay_i + b)$ is transformed into a PWM signal $PWM(\gamma(ay_i + b))$ by the pulse-width modulator to determine the angle of the roll axis of the i-th leg. The set of VHDL codes describing the Hopf CPG model, pulse-width modulators, and saturator is compiled by the same design software environment that was used to compile the proposed CPG model. It is implemented by the same FPGA device that was used to implement the proposed CPG model. The bit length of the Hopf CPG model is shortened based on the same criteria as that of the proposed CPG model. It is then confirmed that the Hopf CPG model realizes the target phase-locking pattern. Features of the Hopf CPG model are summarized in Table 3. Note that the Hopf CPG model that is implemented in the FPGA can be regarded as a hardware digital signal processor (DSP), which is customized to execute the dynamic equation in Eq. (17).

2) PROPOSED CPG MODEL IMPLEMENTED AS SOFTWARE RUNNING ON CUSTOMIZED CPU

For comparison, the proposed CPG model is implemented as a software running on a customized CPU as follows. Using the same design software environment used to design the proposed CPG model, a soft-core CPU called Microblaze [41] is custom designed to execute the dynamic equations in Eqs. (3), (4), (6), (7), (10), (12), and (13) of the presented CPG model. In this design, unnecessary units (e.g., floating point unit and integer multiplier) to execute the dynamic equations are not included in the CPU and the predefined configuration is selected as "application preset," which is among the most standard predefined configurations. The resulting customized CPU is implemented by the same FPGA device used to implement the proposed CPG model. Further, the dynamic equations of the proposed CPG model are written in C-language code, the code is compiled by a compiler embedded in the design software environment used to compile the presented CPG model, and the resulting executable file is downloaded to the customized CPU with the FPGA. It is then confirmed that the CPU-based CPG model realizes the target phase-locking pattern. Features of the CPU-based CPG model are summarized in Table 3.

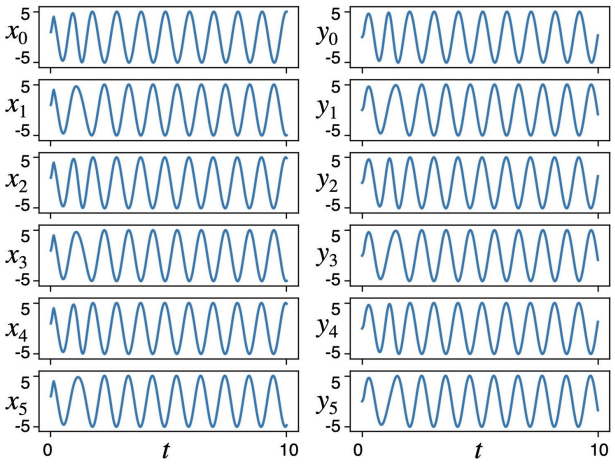

FIGURE 18. Time waveforms of the Hopf CPG model [3]. $\mu_i = 5^2$ and $\xi_i = 2\pi$ for all i. $h = 2^{-5}$.

3) OUR PREVIOUSLY REPORTED CPG MODEL

Our previously reported CPG model [33] is designed by the same design software environment used to design the proposed CPG model and is implemented by the same FPGA device used to implement the proposed CPG model. The differences between the previously reported and proposed CPG model are (a) the previous model has more clocks and flip-flops that do not play any important roles to realize the target phase-locking pattern, and (b) the previous model has more complicated network topology. Features of the previous model with the FPGA are summarized in Table 3.

4) DISCUSSIONS

- Table 3 shows that the proposed CPG model employs the least number of circuit elements and the lowest power compared to the other models. However, the number of flip-flops of the proposed model is slightly higher than that of the Hopf CPG model. This exception can be ignored as the number of circuit elements required to

implement a flip-flop is much smaller than the number of circuit elements required to implement a look-up-table.

- The number of circuit elements employed depends on the optimization algorithm of the design software while the power consumption depends on the process rule of the target device. In this study, the proposed model and other models are designed and compiled by the same design software and implemented by the same FPGA device. Hence, it can be said that the comparisons were appropriate. This is an advantage of the FPGA-based prototype design [42], [43]. In addition, the capability to analyze the specifications of customized processors (e.g., the customized DSP and CPU analyzed in this study) is another advantage of the FPGA-based prototype design.
- The FPGA is further advantageous in designing an advanced CPG model. An advanced hexapod robot requires to change its gate patterns dynamically, and thus, an advanced CPG model requires to change its coupling pattern dynamically to change the phase-locking patterns. A dynamically reconfigurable FPGA is suitable to implement such dynamically reconfigurable neuromorphic hardware [22]. However, such an advanced function of the CPG model is out of the scope of this study as we focused on fundamental studies, e.g., the detailed analyses of the nonlinear dynamics of the CPG model (Sections II and III), the detailed analyses of roles of the asynchronous clocks (Sections II and IV), development of the systematic design method of the CPG model based on the analyses results (Section IV), and implementation of the prototype and comparisons with other models (Section V). Design of a *dynamically reconfigurable CPG model based on the dynamically reconfigurable FPGA* is an important future challenge.

VI. CONCLUSION

This paper presented a novel CPG model consisting of a network of CA oscillators. The detailed analyses showed the effects of the parameters on the nonlinear characteristics of the CA oscillator and its network, such as amplitude of oscillation, frequency of oscillation, phase-locking between the CA oscillators, mean phase difference between the phase-locked CA oscillators, and transient period to the phase-locking. Moreover, the detailed analyses confirmed: *the asynchronous network of asynchronous CA oscillators* is best suited to be used as the CPG to realize the bio-inspired tripod gait of the hexapod robot when compared with the other three types of networks. Using these results, we proposed the systematic design procedures of the proposed CPG model to realize the tripod gait. Then, the CPG model designed by the proposed procedures was implemented in the FPGA, and its operation was verified through experiments. It was shown that the proposed CPG model employs much fewer circuit elements and lower power than the conventional CPG model. Future scope for research is as follows: (a) detailed analyses of various nonlinear dynamics of the proposed CPG model, (b) realization of other gaits of the hexapod robot based on the proposed CPG model, (c) development of further hardware-efficient CPG model based on dimension reduction techniques, and (d) development of a dynamically reconfigurable CPG model based on the dynamically reconfigurable FPGA.

REFERENCES

[1] S. Grillner, "Neurobiological bases of rhythmic motor acts in vertebrates," *Science*, vol. 228, no. 4696, pp. 143–149, Apr. 1985.

[2] A. J. Ijspeert, "Central pattern generators for locomotion control in animals and robots: A review," *Neural Netw.*, vol. 21, no. 4, pp. 642–653, May 2008.

[3] J. Yu, M. Tan, J. Chen, and J. Zhang, "A survey on CPG-inspired control models and system implementation," *IEEE Trans. Neural Netw. Learn. Syst.*, vol. 25, no. 3, pp. 441–456, Mar. 2014.

[4] R. R. Torrealba, J. Cappelletto, L. Fermín, G. Fernández-López, and J. C. Grieco, "Cybernetic knee prosthesis: Application of an adaptive central pattern generator," *Kybernetes*, vol. 41, nos. 1–2, pp. 192–205, Mar. 2012.

[5] R. J. Vogelstein, F. V. G. Tenore, L. Guevremont, R. Etienne-Cummings, and V. K. Mushahwar, "A silicon central pattern generator controls locomotion *in vivo*," *IEEE Trans. Biomed. Circuits Syst.*, vol. 2, no. 3, pp. 212–222, Sep. 2008.

[6] N. Sasagawa, K. Tani, T. Imamura, and Y. Maeda, "Quadruped locomotion patterns generated by desymmetrization of symmetric central pattern generator hardware network," *IEICE Trans. Fundam. Electron., Commun. Comput. Sci.*, vol. E101.A, no. 10, pp. 1658–1667, Oct. 2018.

[7] I. Köymen and E. M. Drakakis, "Current-input current-output analog half center oscillator and central pattern generator circuits with memristors," *Int. J. Circuit Theory Appl.*, vol. 46, no. 7, pp. 1294–1310, Jul. 2018.

[8] F. Li, A. Basu, C.-H. Chang, and A. H. Cohen, "Dynamical systems guided design and analysis of silicon oscillators for central pattern generators," *IEEE Trans. Circuits Syst. I, Reg. Papers*, vol. 59, no. 12, pp. 3046–3059, Dec. 2012.

[9] H. Soleimani, A. Ahmadi, M. Bavandpour, and O. Sharifipoor, "A generalized analog implementation of piecewise linear neuron models using CCII building blocks," *Neural Netw.*, vol. 51, pp. 26–38, Mar. 2014.

[10] L. Minati, M. Frasca, N. Yoshimura, and Y. Koike, "Versatile locomotion control of a hexapod robot using a hierarchical network of nonlinear oscillator circuits," *IEEE Access*, vol. 6, pp. 8042–8065, 2018.

[11] N. Korkmaz, İ. Öztürk, and R. Kılıç, "The investigation of chemical coupling in a HR neuron model with reconfigurable implementations," *Nonlinear Dyn.*, vol. 86, no. 3, pp. 1841–1854, Nov. 2016.

[12] Y. Maeda, T. Hiramatsu, S. Miyoshi, and H. Hikawa, "Pulse coupled oscillator with learning capability using simultaneous perturbation and its FPAA implementation," in *Proc. ICCAS-SICE*, 2009, pp. 3142–3145.

[13] C. Mayr, J. Partzsch, M. Noack, S. Hänzsche, S. Scholze, S. Höppner, G. Ellguth, and R. Schüffny, "A biological-realtime neuromorphic system in 28 nm CMOS using low-leakage switched capacitor circuits," *IEEE Trans. Biomed. Circuits Syst.*, vol. 10, no. 1, pp. 243–254, Feb. 2016.

[14] X. Li, H. Liu, X. Wu, R. Li, and X. Wang, "Improved CPG model based on Hopf oscillator for gait design of new type of hexapod robot," in *Proc. Int. Conf. Intell. Robot. Appl.*, in Lecture Notes in Computer Science, H. Yu, J. Liu, L. Liu, Z. Ju, Y. Liu, and D. Zhou, Eds., vol. 11741, 2019, pp. 72–83.

[15] B. Xu, W. Li, Y. Ni, H. Chi, and W. Ouyang, "Adaptive locomotion generation for a bionic hexapod robot," in *Proc. 45th Annu. Conf. IEEE Ind. Electron. Soc. (IECON)*, Oct. 2019, pp. 5173–5178.

[16] B. Zhong, S. Zhang, M. Xu, Y. Zhou, T. Fang, and W. Li, "On a CPG-based hexapod robot: AmphiHex-II with variable stiffness legs," *IEEE/ASME Trans. Mechatronics*, vol. 23, no. 2, pp. 542–551, Apr. 2018.

[17] E. I. Guerra-Hernandez, A. Espinal, P. Batres-Mendoza, C. H. Garcia-Capulin, R. De J. Romero-Troncoso, and H. Rostro-Gonzalez, "A FPGA-based neuromorphic locomotion system for multi-legged robots," *IEEE Access*, vol. 5, pp. 8301–8312, 2017.

[18] A. Crespi, A. Badertscher, A. Guignard, and A. J. Ijspeert, "AmphiBot I: An amphibious snake-like robot," *Robot. Auton. Syst.*, vol. 50, no. 4, pp. 163–175, Mar. 2005.

[19] A. Zahedi, S. Haghiri, and M. Hayati, "Multiplierless digital implementation of time-varying FitzHugh–Nagumo model," *IEEE Trans. Circuits Syst. I, Reg. Papers*, vol. 66, no. 7, pp. 2662–2670, Jul. 2019.

[20] K. Takeda and H. Torikai, "A novel asynchronous CA neuron model: Design of neuron-like nonlinear responses based on novel bifurcation theory of asynchronous sequential logic circuit," *IEEE Trans. Circuits Syst. I, Reg. Papers*, vol. 67, no. 6, pp. 1989–2001, Jun. 2020.
[21] T. Matsubara and H. Torikai, "Asynchronous cellular automaton-based neuron: Theoretical analysis and on-FPGA learning," *IEEE Trans. Neural Netw. Learn. Syst.*, vol. 24, no. 5, pp. 736–748, May 2013.
[22] T. Matsubara, H. Torikai, and T. Hishiki, "A generalized rotate-and-fire digital spiking neuron model and its on-FPGA learning," *IEEE Trans. Circuits Syst. II, Exp. Briefs*, vol. 58, no. 10, pp. 677–681, Oct. 2011.
[23] T. Hishiki and H. Torikai, "A novel rotate-and-fire digital spiking neuron and its neuron-like bifurcations and responses," *IEEE Trans. Neural Netw.*, vol. 22, no. 5, pp. 752–767, May 2011.
[24] K. Takeda and H. Torikai, "A novel hardware-efficient cochlea model based on asynchronous cellular automaton dynamics: Theoretical analysis and FPGA implementation," *IEEE Trans. Circuits Syst. II, Exp. Briefs*, vol. 64, no. 9, pp. 1107–1111, Sep. 2017.
[25] H. Ishimoto, M. Izawa, and H. Torikai, "A novel cochlea partition model based on asynchronous bifurcation processor," *IEICE Nonlinear Theory Appl.*, vol. 6, no. 2, pp. 207–225, 2015.
[26] M. Izawa and H. Torikai, "Asynchronous cellular automaton model of spiral ganglion cell in the mammalian cochlea: Theoretical analyses and FPGA implementation," *IEICE Trans. Fundam. Electron., Commun. Comput. Sci.*, vol. E98.A, no. 2, pp. 684–699, 2015.
[27] T. Noguchi and H. Torikai, "Ghost stochastic resonance from an asynchronous cellular automaton neuron model," *IEEE Trans. Circuits Syst. II, Exp. Briefs*, vol. 60, no. 2, pp. 111–115, Feb. 2013.
[28] T. Yoshimoto and H. Torikai, "A novel hardware-efficient gene network model based on asynchronous cellular automaton dynamics," *IEICE Nonlinear Theory Appl.*, vol. 8, no. 4, pp. 302–318, 2017.
[29] T. Naka and H. Torikai, "A novel generalized hardware-efficient neuron model based on asynchronous CA dynamics and its biologically plausible on-FPGA learnings," *IEEE Trans. Circuits Syst. II, Exp. Briefs*, vol. 66, no. 7, pp. 1247–1251, Jul. 2019.
[30] T. Matsubara and H. Torikai, "An asynchronous recurrent network of cellular automaton-based neurons and its reproduction of spiking neural network activities," *IEEE Trans. Neural Netw. Learn. Syst.*, vol. 27, no. 4, pp. 836–852, Apr. 2016.
[31] K. Isobe and H. Torikai, "A novel hardware-efficient asynchronous cellular automaton model of spike-timing-dependent synaptic plasticity," *IEEE Trans. Circuits Syst. II, Exp. Briefs*, vol. 63, no. 6, pp. 603–607, Jun. 2016.
[32] N. Shimada and H. Torikai, "A novel asynchronous cellular automaton multicompartment neuron model," *IEEE Trans. Circuits Syst. II, Exp. Briefs* vol. 62, no. 8, pp. 776–780, Aug. 2015.
[33] K. Takeda and H. Torikai, "A novel hardware-efficient CPG model for a hexapod robot based on nonlinear dynamics of coupled asynchronous cellular automaton oscillators," in *Proc. Int. Joint Conf. Neural Netw. (IJCNN)*, 2019, pp. 1–8.
[34] K. Takeda and H. Torikai, "A novel hardware-efficient CPG model based on asynchronous cellular automaton," *IEICE Electron. Express*, vol. 15, no. 11, 2018, Art. no. 20180387.
[35] M. Bavandpour, H. Soleimani, S. Bagheri-Shouraki, A. Ahmadi, D. Abbott, and L. O. Chua, "Cellular memristive dynamical systems (CMDS)," *Int. J. Bifurcation Chaos*, vol. 24, no. 5, May 2014, Art. no. 1430016.
[36] M. Gholami and S. Saeedi, "Digital cellular implementation of Morris–Lecar neuron model," in *Proc. 23rd Iranian Conf. Electr. Eng.*, May 2015, pp. 1235–1239.
[37] D. M. Wilson, "Insect walking," *Annu. Rev. Entomol.*, vol. 11, no. 1, pp. 103–122, 1966.
[38] Lynxmotion. *Mini-Hex Combo Kit for FlowBotics Studio (MH2F)*. Accessed: Jul. 30, 2020. [Online]. Available: http://www.lynxmotion.com/
[39] Xilinx Inc. *Xilinx's FPGA 612 Artix-7 XC7A100T-1CSG324C*. Accessed: Jul. 30, 2020. [Online]. Available: http://www.xilinx.com/
[40] Digilent Inc. *Digilent's Nexys 4 DDR Evaluation Platform*. Accessed: Jul. 30, 2020. [Online]. Available: http://www.digilentinc.com/
[41] P. B. Minev and V. S. Kukenska, "Implementation of soft-core processors in FPGAs," in *Proc. Int. Sci. Conf.*, 2001, pp. 1–4.
[42] R. Bani-Hani, S. Harb, K. Mhaidat, and E. Taqieddin, "High-throughput and area-efficient FPGA implementations of data encryption standard (DES)," *Circuits Syst.*, vol. 5, no. 3, pp. 45–56, 2014.
[43] M. A. Mohsin and D. G. Perera, "An FPGA-based hardware accelerator for K-nearest neighbor classification for machine learning on mobile devices," in *Proc. 9th Int. Symp. Highly-Efficient Accel. Reconfigurable Technol.*, Jun. 2018, pp. 1–7.

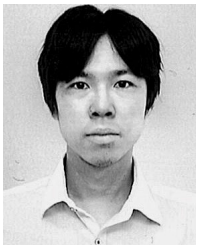

KENTARO TAKEDA (Graduate Student Member, IEEE) received the bachelor's degree in computer science and engineering and the master's degree in frontier informatics from Kyoto Sangyo University, Kyoto, Japan, in 2017 and 2019, respectively. He is currently pursuing the Ph.D. degree with the Graduate School of Engineering Science, Hosei University, Tokyo. His current research interests include nonlinear dynamics, neuromorphic engineering, and digital circuit design.

HIROYUKI TORIKAI (Member, IEEE) received the B.E., M.E., and Ph.D. degrees in electrical engineering from Hosei University, Tokyo, Japan, in 1995, 1997, and 1999, respectively. He is currently a Professor at the Faculty of Science and Engineering, Hosei University. His current research interests include nonlinear dynamics, neural networks, and discrete state dynamics.